Local electronic structure analysis by site-selective ELNES using electron channeling and first-principles calculations

2009 J. Phys.: Condens. Matter 21 104213

(http://iopscience.iop.org/0953-8984/21/10/104213)

IOP PUBLISHING JOURNAL OF PHYSICS: CONDENSED MATTER

J. Phys.: Condens. Matter **21** (2009) 104213 (14pp) doi:10.1088/0953-8984/21/10/104213

Local electronic structure analysis by site-selective ELNES using electron channeling and first-principles calculations

Kazuyoshi Tatsumi[1] **and Shunsuke Muto**

Department of Materials, Physics and Energy Engineering, Nagoya University, Chikusa, Nagoya 464-8603, Japan

E-mail: k-tatsumi@nucl.nagoya-u.ac.jp

Received 15 September 2008, in final form 8 December 2008
Published 10 February 2009
Online at stacks.iop.org/JPhysCM/21/104213

Abstract

In this paper, we review our recent analyses of electron energy loss near edge structure (ELNES) of particular crystalline sites, exploiting dynamical electron diffraction effects, or electron channeling, whereby the excitation weights of the Bloch waves propagating in a crystal can be controlled systematically by adjusting the diffraction conditions. A state-of-the-art data processing technique, multivariate curve resolution (MCR), can restore purely site-specific spectral profiles and their compositions from the experimental data set. Another technique, the Pixon deconvolution method, effectively removes the statistical noise, which enables us to compare the spectral fine structures with those calculated by first principles and discuss the site-specific local atomic and electronic structures. We demonstrate typical case studies in model materials and then an advanced chemical state analysis in a real material. Finally, some remarks toward further refinement of the method are made.

(Some figures in this article are in colour only in the electronic version)

1. Introduction

With the recent advances in (scanning) transmission electron microscopes ((S)TEMs) and related analytical instruments, lateral spatial resolution has attained an atomic scale for imaging and chemical analysis. The mainstream STEM instrumentation aims to make a finer and more intense electron probe by improving the electron gun optics and electron source design. The minimum source size available now is as small as 50 pm, which in principle enables not only atomic column by column analysis but also even the electronic states localized between atomic columns. However, these measurements inevitably require a high-energy dense electron flux to concentrate on the sample thin foil, and thus sometimes cause serious radiation damage and deteriorate the sample, which limits the applicability of these methods.

One of the alternative ways to probe atomically localized electronic states by analytical (S)TEM is to utilize amplitude modulations of electron wavefunctions propagating in a crystal, a clever method for atomic scale analysis that does not necessitate focusing of the electron beam onto the sample: in crystalline materials, high-energy electrons behave as Bloch waves, the symmetries, and amplitudes of which can be controlled by selecting an appropriate set of Bragg reflections and the excitation error of each reflection in a TEM. Let us assume the two-beam excitation condition shown in figure 1(a), where only one reciprocal point (Bragg reflection) is strongly excited. Under this condition, the incident electron wavefunction is divided into two Bloch states, whose wavenumbers are confined on closely separated branches (energy levels), called dispersion planes. The two Bloch states are characterized by the same periodicity, compatible with that of the Bragg reflecting planes, and a phase difference of π from each other, in the direction parallel to the diffracting vector, $\mathbf{g} = (hkl)$. In a simple orthogonal monatomic lattice, one of the Bloch waves propagates through the crystal with its intensity maxima lying on the (hkl) planes, while the other

[1] Author to whom any correspondence should be addressed.

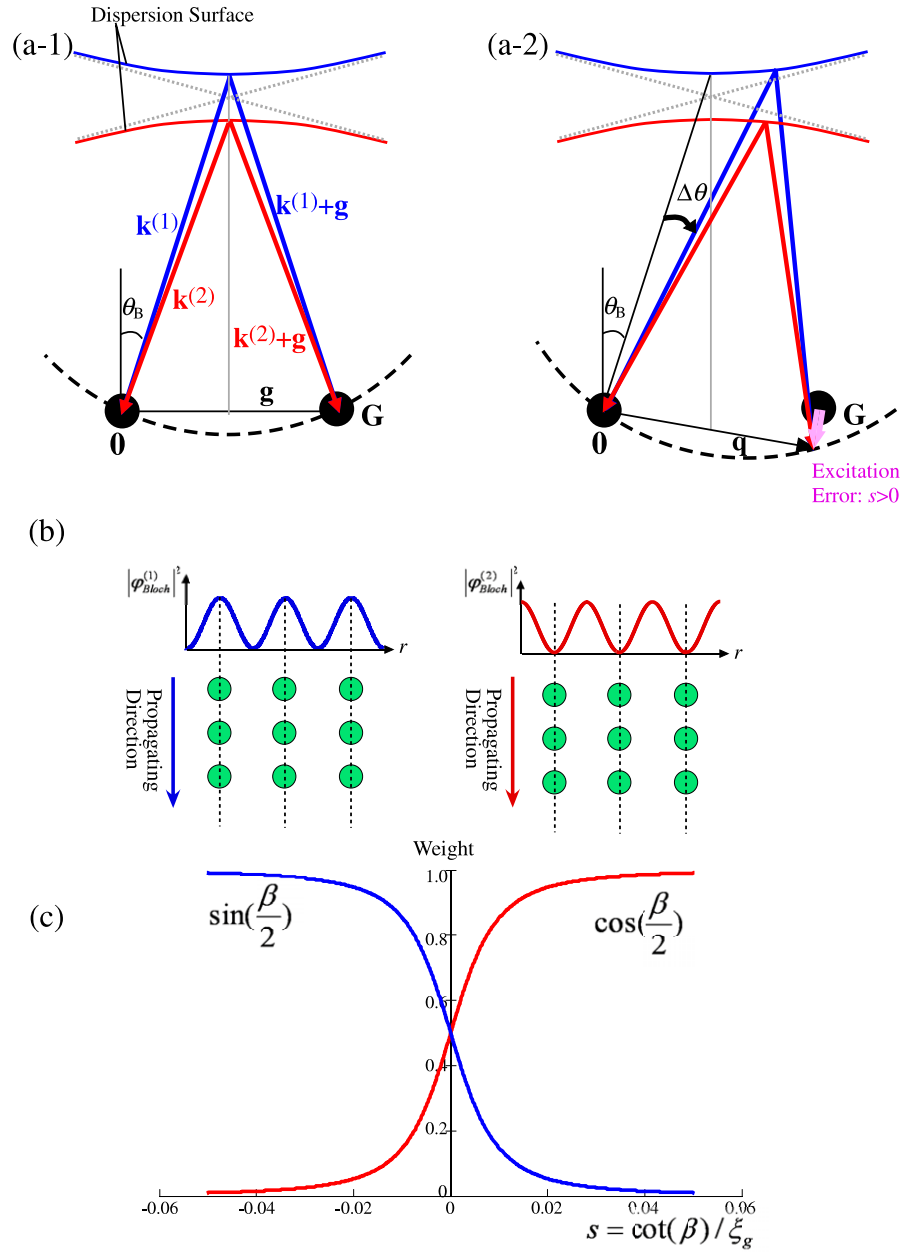

Figure 1. Reciprocal constructions for two-beam excitation conditions, satisfying the exact Bragg condition for **g** (a-1) and slightly deviating from it with a positive excitation error, $s > 0$ (a-2). Bloch waves correspond to the wavevectors $\mathbf{k}^{(1)}$ and $\mathbf{k}^{(2)}$ (b), and their weights (excitation parameters) with respect to the excitation errors (c).

Bloch wave propagates with its intensity maxima kept just in between the (hkl) planes, as shown in figure 1(b). The total wavefunction is the linear combination of the two Bloch waves $\varphi^{(1)}_{\mathrm{Bloch}}$ and $\varphi^{(2)}_{\mathrm{Bloch}}$ with these coefficients:

$$\Psi(r) = \sin\left(\frac{\beta}{2}\right)\varphi^{(1)}_{\mathrm{Bloch}}\left(k^{(1)}, r\right) + \cos\left(\frac{\beta}{2}\right)\varphi^{(2)}_{\mathrm{Bloch}}\left(k^{(2)}, r\right). \quad (1)$$

The parameter β is related to the diffraction condition by $g\xi_g \tan(\Delta\theta) = s\xi_g = \cot(\beta)$, where ξ_g is the extinction distance of the operating Bragg reflection **g**, and the other parameters are illustrated in figure 1(a). The changes in the excitation parameters, $\sin(\beta/2)$ and $\cos(\beta/2)$ for Bloch waves (1) and (2), respectively, which are weighting coefficients that represent to what degree each Bloch wave is excited, are plotted as a function of s in figure 1(c). One can thus localize the Bloch waves along specific atom planes/columns by setting s to be positive or negative around a certain Bragg condition. This phenomenon is known as the electron channeling effect.

This effect has been utilized in ALCHEMI (atom location by channeling enhanced microanalysis) mainly for energy dispersion x-ray analysis (EDX). ALCHEMI can be extended to atom site-selective electronic state analysis when applied to TEM-EELS (electron energy loss spectroscopy), which has barely been reported [1, 2]. Taftø *et al* were the first to report an analysis of this type [3]. They studied the

valence of iron ions in a chromite spinel. Although channeling EELS has the potential of site-specific measurements in crystals, few applications have been reported [4, 5]. To the authors' best knowledge, there have been no chemical state analyses other than that of Taftø *et al* and our recent report [6]. One of the reasons for this is that the signal-to-noise ratio usually could be very low under the channeling conditions because the EELS entrance aperture should be placed off-axis under the two-beam excitation condition [3], and this could smear out the fine features of ELNES. Another reason was the lack of a reliable theoretical calculation for interpreting ELNES. To overcome the first difficulty, several algorithms to deconvolve the raw spectra are now available. They restore the spectra with the S/N ratio and the instrumental energy spread is much improved [7–9]. The second difficulty has been overcome by the recent first-principles calculations that have been reported to successfully reproduce ELNES [10].

In this paper, we demonstrate the atomic site-specific analyses of ELNES under electron channeling conditions. This paper consists of six sections. The section after this introduction describes the theoretical framework of site-selective EELS on the basis of dynamical electron scattering theory combined with inelastic electron scattering theory. In section 3, two typical case studies are presented to show how site-selective EELS measurements are actually carried out, and the results are compared with theoretical spectral predictions. In section 4, several effective data processing techniques are introduced, and these are applied to one of the actual cases to discuss the site-specific electronic structures, which are interpreted using the theoretical spectra obtained through first principles. Section 5 demonstrates more advanced applications of the present method. Finally, we summarize the results obtained and describe the future prospects of the method.

2. General theory for site-selective EELS

In section 1, the two-beam dynamical electron diffraction theory was employed to calculate the explicit strength of the Bragg spots, but the inelastic scattering intensities were treated by an incoherent superposition of intensities from the respective Bloch waves. This treatment is called the 'kinematical coupling' approach [13], which considers Bragg reflection of the fast electron before inelastic interaction but neglects it afterward. In the present section, a dynamical approach is introduced for electron channeling based on the Schattschneider's formulation [13]. This approach describes the fast electron as a Bloch wave field both before and after the inelastic event. Let us suppose our experimental configuration is as shown in figure 1(a), where a Bragg reflection, **g**, is strongly excited. An EEL spectral intensity is expressed by the following double-differential cross-section [11]:

$$\frac{\partial^2\sigma}{\partial E\partial\Omega} = \frac{4\gamma^2}{q^4a_0^2}\frac{k}{k_0}S(\mathbf{q},\mathbf{q}',E), \tag{2}$$

which is the probability that the incident electron losing its kinetic energy between E and $E+\Delta E$ is scattered within the solid angle $\Delta\Omega$ subtended by the detector entrance aperture located at the position specified by $\mathbf{q}$ and $\mathbf{q}'$. In equation (2), k_0 and k are the wavenumbers of the incident and scattered electrons, respectively, γ is the relativistic correction factor, and a_0 is the Bohr radius. The momentum transfer vectors $\mathbf{q}$ and $\mathbf{q}'$ are defined by

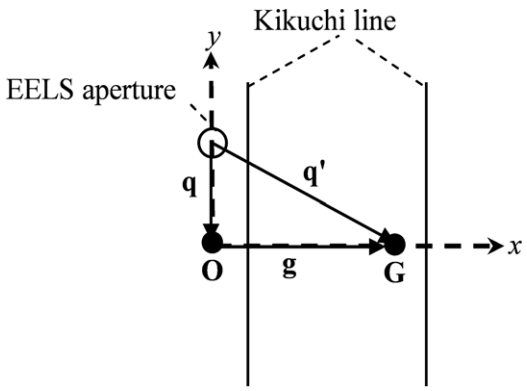

Figure 2. Experimental geometry of diffraction pattern for site-selective EELS.

$$\mathbf{q} = \mathbf{k}_0 - \mathbf{k}, \qquad \mathbf{q}' = \mathbf{q} + \mathbf{g}. \tag{3}$$

$S(\mathbf{q},\mathbf{q}',E)$ is a so-called mixed dynamical form factor (MDFF), expressible for an N-electron system as [12]

$$S(\mathbf{q},\mathbf{q}',E) = \sum_i p_i \sum_f (1-p_f) \sum_j^N \langle i|\exp(\mathrm{i}\mathbf{q}\cdot\mathbf{r}_j)|f\rangle \times \sum_{j'}^N \langle \mathrm{i}|\exp(\mathrm{i}\mathbf{q}'\cdot\mathbf{r}_{j'})|f\rangle \delta(E+E_i-E_f), \tag{4}$$

where $\langle i|$ and $|f\rangle$ are the initial and final states of electrons associated with electron transitions from the initial energy level E_i to the final level E_f, and p_i and p_f are the occupancies of the ith initial state and fth final state, respectively. The summation with respect to j and j' is taken over the coordinates of the excited electrons. To discuss the electron channeling effects under a specific Bragg condition, we have to take the dynamical scattering of the incident and emerging fast electron using Bloch waves. This approach has already been used by Schattschneider *et al* based on the distorted-wave Bloch approximation [12], and the final expression for the double-differential scattering cross-section for inelastic scattering can be given in the following form under the geometrical configuration shown in figure 2, taking into account the absorption effect phenomenologically [13, 14]:

$$\frac{\partial^2\sigma}{\partial E\partial\Omega} \propto \langle\varphi_f|\langle f|V(\mathbf{q})|i\rangle|\varphi_i\rangle\langle\varphi_i|\langle i|V(\mathbf{q}')|f\rangle|\varphi_f\rangle \times \delta(E+E_i-E_f) \propto \sum_{jj'}\sum_{gg'}\sum_{ll'}\sum_{hh'} K_{gg'hh'}T_{jj'll'}(t) \times u_g^{(j)}u_{g'}^{(j')*}v_h^{(l)}v_{h'}^{(l')*}\frac{\mathbf{q}\cdot\mathbf{q}'}{q^2q'^2}\delta(E+E_i-E_j), \tag{5}$$

where

$$K_{gg'hh'} = \sum_{\mathbf{u}}^{\text{unitcell}} \mathrm{e}^{\mathrm{i}(\mathbf{g}-\mathbf{h}-\mathbf{g}'+\mathbf{h}')\cdot\mathbf{u}},$$

$$T_{jj'll'} = \frac{\cosh\left(\delta\eta\frac{t}{2}\right)\sin\left(\Delta\frac{t}{2}\right) + i\sinh\left(\delta\eta\frac{t}{2}\right)\cos\left(\Delta\frac{t}{2}\right)}{\Delta\frac{t}{2} + \mathrm{i}\delta\eta\frac{t}{2}}, \quad (6)$$

$$u_g^{(j)} = C_0^{(j)} C_g^{(j)},\ v_h^{(l)} = D_0^{(l)} D_g^{(l)}$$

$C_g^{(i)}$ and $D_g^{(i)}$ are Fourier components of the ith branch of the incident ($|\varphi_i\rangle$) and outgoing ($|\varphi_f\rangle$) Bloch waves (corresponding to the Bragg reflection, $\mathbf{g}$) before and after the inelastic scattering, respectively. $\mathbf{q}$ and $\mathbf{q}'$ are now the momentum transfer vectors pointing to the entrance aperture of the EELS detector from the origin and $\mathbf{g}$, respectively, and t is the sample thickness. The last term in equation (5) corresponds to the dipole transition approximation,

$$S(\mathbf{q}, \mathbf{q}', E) \propto \mathbf{q}\cdot\mathbf{q}'\delta(E + E_i - E_f), \quad (7)$$

as given in [12]. $K_{gg'hh'}$ is a kind of structure factor resulting from the summation over the atomic positions in the unit cell, which determines the site-selectivity of the propagating Bloch waves. $T_{jj'll'}$ is a thickness-dependent function denoting the absorption effects, where

$$\begin{aligned} \Delta &= \gamma^{(j)} - \gamma^{(j')} - (\gamma^{(l)} - \gamma^{(l')}), \\ \delta\eta &= \eta^{(j)} - \eta^{(j')} - (\eta^{(l)} - \eta^{(l')}), \end{aligned} \quad (8)$$

and $\gamma^{(j)}$ and $\eta^{(j)}$ are, respectively, the real and imaginary parts of the jth eigenvalue of the dynamical diffraction theory (propagation vector of the jth Bloch wave).

In the two-beam approximation, the fast-electron Bloch states are analytically obtained as [15]

$$C_0^{(1)} = C_g^{(2)} = \cos\frac{\beta}{2}, \qquad C_0^{(2)} = -C_g^{(1)} = \sin\frac{\beta}{2}, \quad (9)$$
$$w = s\zeta_g = \cot\beta,$$

and

$$\begin{aligned} \gamma^{(1)} &= \left(w - \sqrt{w^2+1}\right)/2\xi_g, \\ \gamma^{(2)} &= \left(w + \sqrt{w^2+1}\right)/2\xi_g \\ \eta^{(1)} &= \left(1 - \frac{1}{\sqrt{1+w^2}}\right)\Big/ 20\xi_g, \\ \eta^{(2)} &= \left(1 + \frac{1}{\sqrt{1+w^2}}\right)\Big/ 20\xi_g \end{aligned} \quad (10)$$

where s is the excitation error and ξ_g is the extinction distance of the operating Bragg reflection $\mathbf{g}$. In the present diffraction geometry, as shown in figure 2, $D_g^{(i)} = C_g^{(i)}$ since the detector aperture located off-axis from the transmitted beam parallel to the Kikuchi line allows the same boundary condition to apply to the outgoing waves after inelastic scattering. The phenomenological absorption is taken into account by introducing the complex extinction distance with the imaginary part $\xi_g' = 20\xi_g$. Then equations (5)–(10) provide the analytical form for simulating the electron channeling EELS under the two-beam condition:

$$\begin{aligned} \frac{\partial^2\sigma}{\partial E\partial\Omega} &\propto \sigma_\pm\Big(-\cos^7\frac{\beta}{2}\sin\frac{\beta}{2} - \cos^5\frac{\beta}{2}\sin^3\frac{\beta}{2} \\ &\quad + \cos^3\frac{\beta}{2}\sin^5\frac{\beta}{2} + \cos\frac{\beta}{2}\sin^7\frac{\beta}{2}\Big) \\ &\quad \times [S(\mathbf{q}, \mathbf{q}+\mathbf{g}, E) + S(\mathbf{q}, \mathbf{q}-\mathbf{g}, E)] \\ &\quad + [\text{site-independent-term}] \\ &\propto \sigma_\pm\Big(-\cos^7\frac{\beta}{2}\sin\frac{\beta}{2} - \cos^5\frac{\beta}{2}\sin^3\frac{\beta}{2} \\ &\quad + \cos^3\frac{\beta}{2}\sin^5\frac{\beta}{2} + \cos\frac{\beta}{2}\sin^7\frac{\beta}{2}\Big) \\ &\quad \times \left[\frac{\mathbf{q}\cdot(\mathbf{q}+\mathbf{g})}{\mathbf{q}^2(\mathbf{q}+\mathbf{g})^2} + \frac{\mathbf{q}\cdot(\mathbf{q}-\mathbf{g})}{\mathbf{q}^2(\mathbf{q}-\mathbf{g})^2}\right] \\ &\quad + [\text{site-independent-term}] \end{aligned} \quad (11)$$

where only the interference term effective for site-selective measurement is left and the thickness-dependent term is omitted for simplicity. $\sigma_\pm = \pm 1$, depending on the atomic site of the element of interest, originating from $K_{gg'hh'}$ in equation (6).

Figure 3 plots $\partial^2\sigma/\partial E\partial\Omega$ for a virtual element located at the octahedral site ($\sigma_\pm = -1$) and tetrahedral site ($\sigma_\pm = 1$) in the spinel structure as a function of the nondimensional excitation error w ($=s\xi_g$) and detector position q_y (see figure 2) with $\mathbf{g} = 400$. The thickness-dependent and q^{-4}-dependent terms are neglected in order that the site-selectivity may be revealed. The signal intensity for both sites switches dramatically from a finite value to nearly zero when the sign of w is reversed. As expected, increasing q_y enhances the site-selectivity. As a matter of fact, the dipole transition approximation is no longer valid for large q_y; a more mathematically precise treatment based on quantum mechanics is necessary for a quantitative discussion, which is beyond the scope of this paper. It should also be mentioned that the signal intensity decreases significantly with increasing q_y, as a result of the q^{-4}-dependent term. Hence, in the actual experimental setup, a compromising condition has to be sought, optimizing the trade-off between the signal intensity and site-selectivity.

The effect of sample thickness, t, is shown in figure 4 for the case of $q_y = 0.2$ and $\sigma_\pm = 1$, where the q^{-4}-dependent terms are again neglected. The dynamical electron diffraction gives rise to an intensity oscillation with sample thickness, with a period equal to the effective extinction distance, $\xi_g/\sqrt{1+w^2}$. The absorption effect dilutes the site-selectivity significantly because the minor component remains largely independent of the diffraction conditions. In principle, the thicker the sample is, the more distinct the site-selectivity becomes; however, the background intensities and multiple-loss effect predominate, which also requires an optimum compromise condition in practice.

3. Case studies

As application examples, we present two case studies for spinel structures, where single metal ions occupy either the

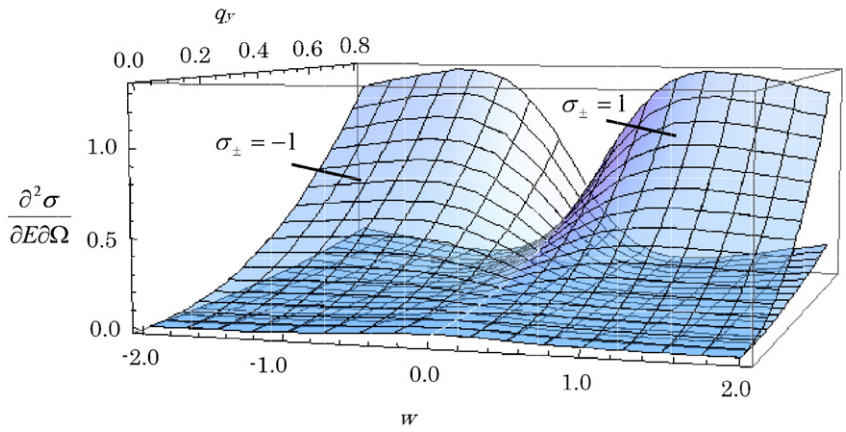

Figure 3. Variation of site-dependent EELS intensities with respect to the deviation from the Bragg condition, w, and the displacement of EELS detector. q_y is the magnitude of **q** in figure 2.

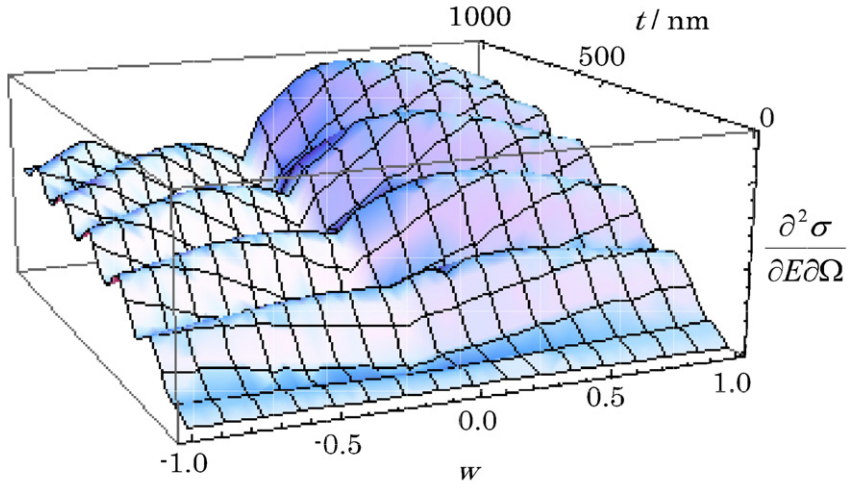

Figure 4. Variation of site-dependent EELS intensities with respect to the sample thickness, t, and the deviation from the Bragg condition, w.

tetrahedral or octahedral site, and are coordinated by four or six oxygen atoms, respectively, as shown in figure 5(a). TEM samples were prepared by ion-milling sintered polycrystalline crystals. To distinguish the two sites, the experiments were conducted at the 400 Bragg condition ($\mathbf{g} = 400$), changing the sign of s. Unless otherwise noted, we used a Jeol JEM-200CX TEM operated at an accelerating voltage of 200 kV, equipped with a Gatan EEL spectrometer Enfina1000. Relatively large convergent and collection angles (approximately 7 and 15 mrad, respectively) were applied with a short camera length (∼20 cm) so as to achieve higher signal intensities. The size and thickness of the illuminated area of the sample were approximately 1 μm and 50–100 nm, respectively. The EELS detector was displaced by approximately 0.6 G along the (400) Kikuchi line to strengthen the localization of the incident electron. Hence, the signal-to-noise ratios (S/N) were quite low, which necessitates relatively long exposure (∼45 s).

The pre-edge background of the raw data was removed using the power law, while the plural scattering effect was not corrected because the intensities did not significantly affect the spectral features near the edge threshold. It should be noted that no appreciable radiation damage associated with the high-energy electron beam was observed during the measurements.

Transition probabilities were calculated within the electric dipole approximation in the first-principles theoretical ELNES calculations. Large momentum transfer vectors (≈**g**) could involve other contributions such as the monopole transition, but a spectral simulation including the large momentum transfer vectors showed that their effects on the spectral shape were small enough to ignore for a qualitative comparison of the theoretical spectra and the site-specific experimental ELNES. The final spectra were broadened by a Gaussian function with a FWHM of 0.6–1.0 eV, depending on the required energy resolution.

3.1. Mn $L_{2,3}$ ELNES of Mn_3O_4

Mn_3O_4 has a normal spinel structure with a tetragonal distortion. The tetrahedral and octahedral sites are occupied by Mn^{2+} and Mn^{3+}, respectively [16, 17]. We measured Mn $L_{2,3}$ ELNES of Mn_3O_4, which are compared with the results of

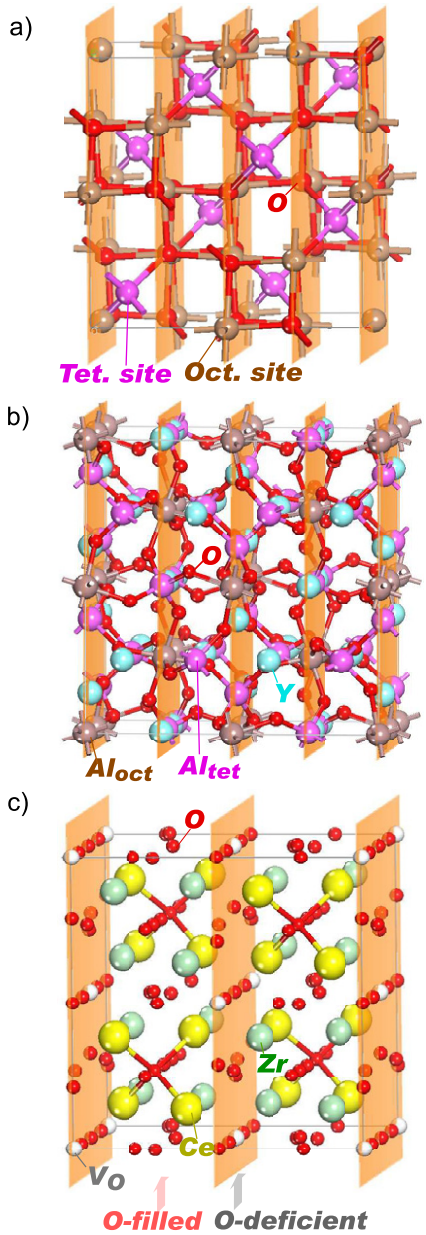

Figure 5. Crystal structures of the materials studied: (a) spinel, (b) $Y_3Al_5O_{12}$ (YAG), and (c) $Ce_2Zr_2O_{7.5}$. Highlighted vertical planes represent the set of planes containing one type of atomic sites. The Bragg spots corresponding to the sets are selected for site-selective EELS experiments.

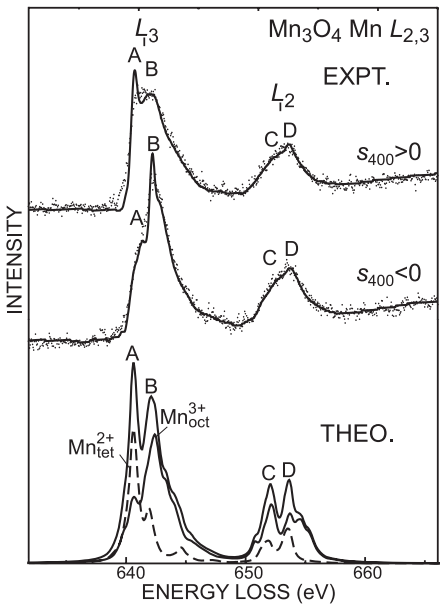

Figure 6. Experimental Mn $L_{2,3}$ ELNES of Mn_3O_4 under (400) channeling conditions (upper) and theoretical spectra of divalent Mn at the tetrahedral site and trivalent Mn at the octahedral site (lower). In the experimental spectra, the dots are the measured data, and the lines are the measured data after noise removal by the Pixon method (described in the text, section 4.1).

the first-principles many-electron calculation in figure 6. We adopted a totally relativistic first-principles molecular orbital calculation [18, 19]. Electronic correlations among the Mn $2p_{1/2}$, $2p_{3/2}$ and 3d electrons were taken into account explicitly as the configuration interaction (CI) incorporated with the Slater determinants of these molecular orbitals. We used $(MnO_4)^{6-}$ and $(MnO_6)^{9-}$ cluster models for Mn^{2+}_{tet} and Mn^{3+}_{oct}, respectively. To take the effective Madelung potential into account, point charges were placed at the external atomic sites. The channeling experiment indicates that the first and second peaks (A and B) are ascribable to Mn_{tet} and Mn_{oct}, respectively, because positive s_{400} localizes the incident electron at the less dense atomic planes of Mn_{tet} according to dynamical theory under the two-beam approximation [20]. The calculated total spectrum has four distinct peaks: A and B at the L_3 edge and C and D at the L_2 edge. The site-specific theoretical spectra indicate that peaks A and B are mainly from Mn^{2+}_{tet} and Mn^{3+}_{oct}, in agreement with the experiment. The indicated charge order is consistent with that reported by neutron diffraction experiments. This example of EELS measurements under channeling conditions suggests that the reliable first-principles calculation of spectra reflecting multiplet structures and the site-probing EELS could provide an effective tool for analyzing the charge ordering of transition metal ions in crystalline materials.

3.2. Al K ELNES of $NiAl_2O_4$

The next example material is $NiAl_2O_4$, which has a partially inverse spinel structure [21]. The spectra in figure 7 were measured at an excitation error of $g = 400$, s_{400}, positive and negative, as in the inset of the corresponding diffraction condition. Again, the low-energy peak enhanced at $s_{400} > 0$ is attributable to Al_{tet}, while the intensities at higher energies are mainly due to Al_{oct}.

The theoretical Al K ELNES at each site was calculated by the first-principles OLCAO (orthogonalized linear combination of atomic orbitals) method [22, 23] based on the density functional theory (DFT) under the local density approximation. Since atomic orbitals are used as basis functions in this method, features that appear in theoretical spectra can be analyzed in terms of the interactions between atomic orbitals in a straightforward manner [22, 24]. Supercells containing 56 atoms with one core-hole Al were

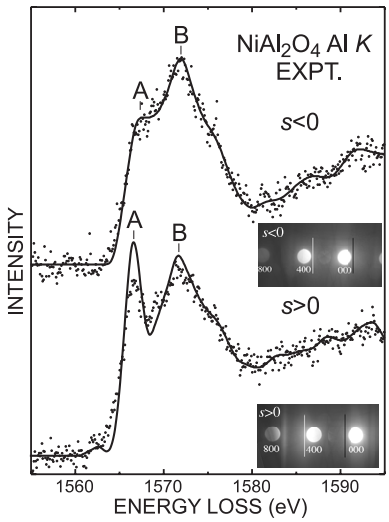

Figure 7. Al K ELNES of $NiAl_2O_4$ under (400) channeling conditions. The dots and lines were obtained as described in the caption of figure 6. In the diffraction pattern insets, white and black lines indicate the location of 400 Kikuchi excess and deficient lines, respectively.

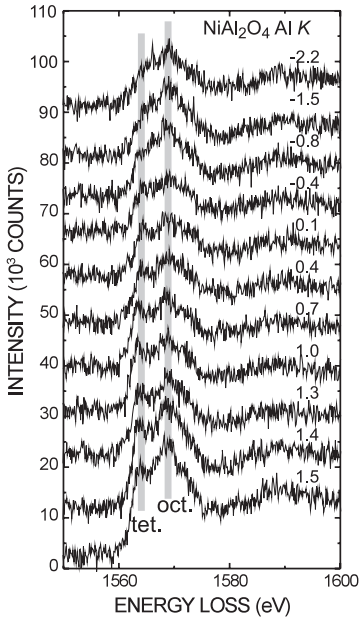

Figure 8. Al K ELNES of $NiAl_2O_4$ under (400) channeling conditions with the excitation error systematically varied. Thick gray lines indicate the location of the main peaks of tetrahedral and octahedral Al. The corresponding deviation parameters $w = s\xi_g$ are shown.

used. Prior to the spectral calculations, the crystal parameters of the spinel were optimized by a different first-principles procedure, namely, the projected augmented-wave (PAW) method [25, 26], to reduce computational cost. In this procedure, Al occupation sites in spinel were optimized within a primitive cell ($Z = 2$) of the cubic spinel. The conditions used for the structural optimization are detailed in [2]. It is seen that the experimental spectra exhibit distinct channeling effects.

4. Further refinement of the method

4.1. Data processing to extract site-specific information

Since the cross-section of each site varies with respect to the excitation error, measured spectra are sum spectra of purely site-specific spectra with different weights, whose values depend on the experimental conditions such as the excitation error and sample thickness, as described in section 2. Given that the systematic data are obtained with just the excitation error varied, we can deduce purely site-specific spectra from them by statistical analysis, e.g., multivariate curve resolution (MCR) [27]. In this procedure, the sum spectra of the different components, the pure spectra, and their weights are represented by the matrices **X**, **S** and **C**. m experimental spectra with n energy bins and l site-specific pure spectral components yield **X** ($n \times m$), **S** ($n \times l$) and **C** ($m \times l$) and $\mathbf{X} = \mathbf{S}\mathbf{C}^T + \mathbf{E}$, where **E** denotes the residual components, not explained by l components. Although one of the most historically well defined techniques in factor analysis is principal component analysis (PCA), extracting an orthogonal set of factors capturing a large amount of variance in a data set, the factors are often difficult to interpret directly because they may not always represent the actual chemical properties, and the resolved spectra are often distorted by the preprocessing and matrix diagonalization procedure. In contrast, the column vectors of **S** in MCR are a set of the pure component spectra resulting from the alternating least-square 'fitting' constrained by some physical properties such as non-negative weights and/or spectral intensities, normalized weights or spectral intensities. Figure 8 shows 11 spectra with different s_{400}, which have **X** (11×600). In the present MCR procedure, the modified alternating least-square (MALS) algorithm [28] was adopted to decompose **X** into **C** and **S** with the non-negative constraint on **S** and **C** and the normalization constraint on each column of **S**.

The low S/N of the measured spectra is another problem that needs to be addressed for site-specific analysis. One solution is to apply a deconvolution technique to remove the statistical noise. In general, an EELS spectrum is given by the convolution of an ideal spectrum and a point-response-function (PRF), which can be obtained by measuring the low-loss spectrum:

$$D(x) = \int_{V_y} \mathrm{d}V_y \, H(x-y) I(y) + N(x), \qquad (12)$$

where $D(x)$ is the observed spectrum, $I(x)$ is the ideal spectrum, $H(x)$ is the PRF and $N(x)$ is the noise. We first applied MCR on the raw data set, and then restored the site-specific signals by deconvolution. We adopted the Pixon algorithm, whose application to EELS was recently developed [29, 30]. It is worth noting that this method adapts itself to the distribution of information content in the data and processes it locally, forming $I(x)$ by convoluting the pseudo-image with smoothing functions, whose scale factor is

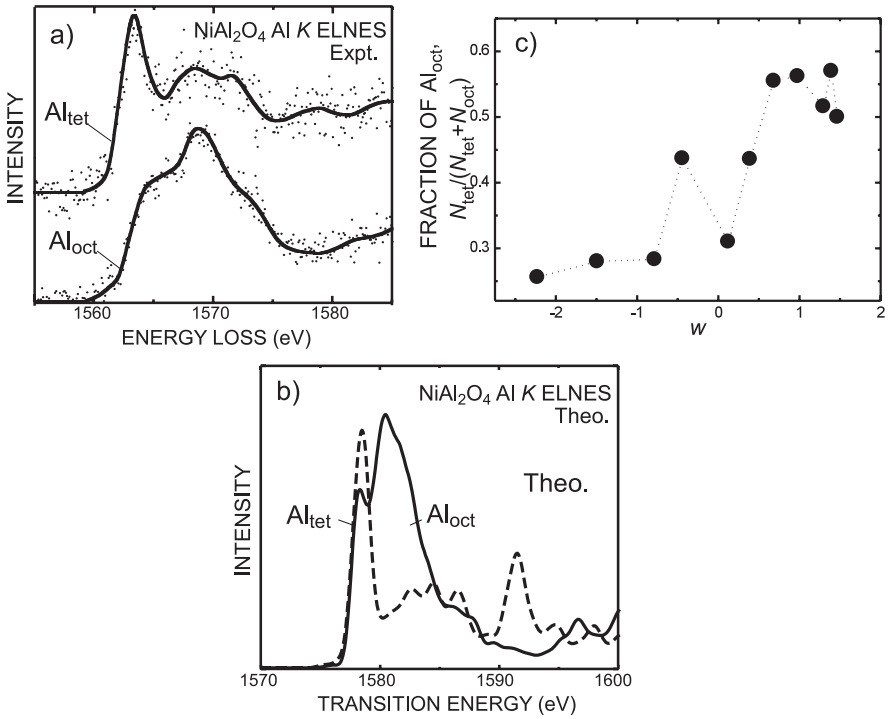

Figure 9. Experimental site-specific Al K ELNES of $NiAl_2O_4$ decomposed by MCR, where the lines are the spectra after noise removal by the Pixon method (a), the corresponding theoretical spectra (b) and the fraction of the tetrahedral signals with respect to w (c).

determined locally.

$$I(x) = \int_{V_y} \mathrm{d}V_y \, K\left(\frac{\|x-y\|}{\delta(x)^2}\right)\phi(y) \qquad (13)$$

where ϕ is the pseudo-image, K is the Pixon kernel and $\delta(x)$ is the scale factor at point x. Because the smoothness of K is optimized location by location, this method avoids regional oversmoothing or undersmoothing, which enables a robust restoration of low S/N data.

The $NiAl_2O_4$ data set in figure 8 shows that the tetrahedral intensities at low energy (1563 eV) and the octahedral intensities at high energy (1569 eV) change systematically as s_{400} decreases. Multiple scattering effects relative to the core-loss intensities would be almost constant with respect to w, because the effective sample thickness changed little with the small tilt angle. We thus neglected the effects in the subsequent procedures. Results of the MCR and Pixon deconvolution for the data (figure 9(a)) are compared with the first-principles theoretical site-specific spectra (figure 9(b)). Comparison of the decomposed spectra with the theoretical ELNES and figure 7 reveals that the ELNES of the individual sites are separated successfully. The other decomposed matrix, **C**, is plotted in figure 9(c), as Al_{tet} weights with respect to $w = s\xi_{400}$. It increases dramatically from 0.3 to 0.6 as w increases from -1 to 1, which is qualitatively consistent with figure 3. Hence, site-selective ELNES measurements are fulfilled in the true sense of the word.

4.2. Site-specific electronic structures of $NiAl_2O_4$

In the experimental site-specific Al K ELNES of $NiAl_2O_4$, the energy position of the main peak of the Al_{oct} spectrum is higher than that of the Al_{tet} spectrum. The theoretical spectra show the same trend. It is believed that the difference in peak positions roughly reflects the difference in local electronic structure around Al_{tet} and Al_{oct}. Figure 10 shows the details of the calculated electronic structure, the local partial densities of states (LPDOSs) and overlap population diagrams (OPDs)[2] of Al_{tet} and Al_{oct} for the non-core-hole, ground state electronic structure, because we intend to correlate the ground state electronic structures with the site-specific peak positions. The Fermi level is set to zero in each figure. In the conduction bands, the Al_{tet} 3p LPDOS in figure 10(a) exhibits a broad dispersion and significant intensities at low energies. By contrast, the 3p LPDOS of the octahedral sites in figure 10(e) is mainly located in the higher-energy region of 8–16 eV. Thus, the conduction-band structure simply explains the site-specific peak positions. The Al_{tet} 3d and 3p LPDOSs in figure 10(a) have peaks at similar energies, 5 eV, 10–13 eV, and 20–21 eV (peaks A, B, C and D in Al_{tet} 3p LPDOS), indicating that 3p and 3d states are significantly hybridized at the tetrahedral site. This is not the case for the Al_{oct} LPDOS in figure 10(e). Given that the local coordinations of Al_{tet} and Al_{oct} correspond approximately to T_d and O_h symmetry, respectively, the p- and d-symmetry orbitals of the same Al could be hybridized only for Al_{tet}. The OPD between Al and its near-neighbor O in figures 10(b) and (c) actually confirm the hybridization. Al_{tet} 3d–O 2p in figure 10(c) as well as Al_{tet} 3p–O 2p in

[2] Local (and partial) density of states (LDOS (and LPDOS)) and overlap population diagram (OPD) are obtained from specific overlap population, whose formulation in the OLCAO method is described in [24]. They are convoluted by a Gaussian function with the same FWHM as the theoretical spectrum.

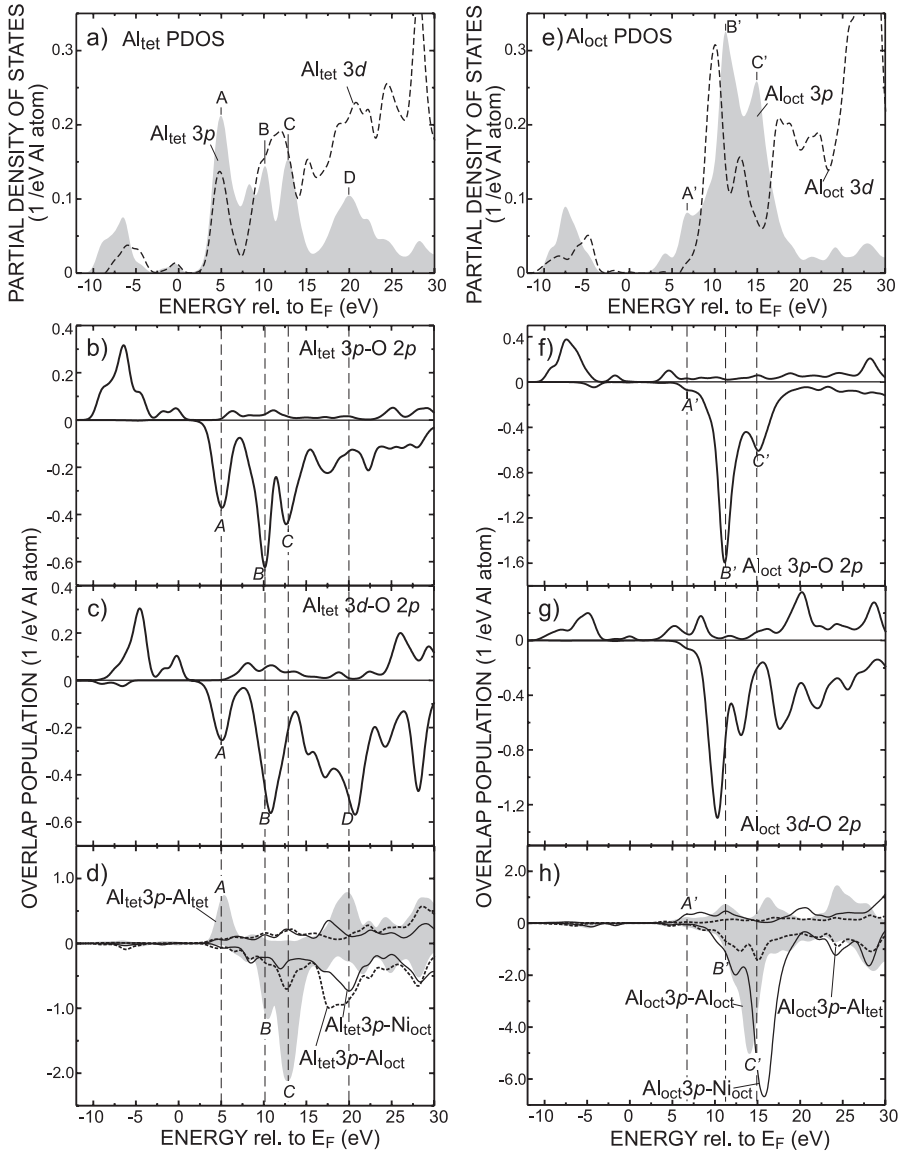

Figure 10. Calculated local partial densities of states and overlap population diagrams of $NiAl_2O_4$ with no holes in Al 1s states. The vertical dashed lines show the energy positions of the characteristic peaks in Al 3p LPDOS.

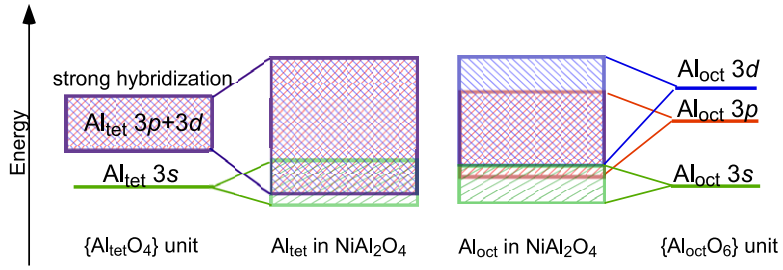

Figure 11. Schematic diagram showing energy levels in the conduction bands, associated with the tetrahedral and octahedral Al in $NiAl_2O_4$.

figure 10(b) show significant anti-bonding-type interactions with good correlation at peaks A and B, while the OPD profiles of Al$_{oct}$ 3d–O 2p and Al$_{oct}$ 3p–O 2p (figures 10(g) and (f)) are not so well correlated.

In order to examine orbital interactions related to Al 3p, we show OPDs between Al$_{tet,oct}$ 3p and the near-neighbor cations in figures 10(d) and (h). Comparing figure 10(d) with 10(a), the lowest-energy peak (peak A) is characterized by bonding interactions between Al$_{tet}$ 3p and its neighboring Al$_{tet}$. Al$_{oct}$ 3p does not form such a purely bonding interaction. Therefore, as schematized in figure 11, the lower energy of Al$_{tet}$ K ELNES could be ascribed to a conduction-band

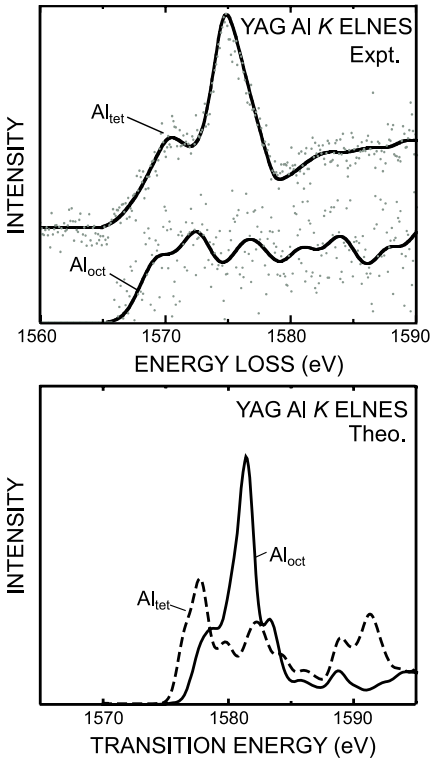

Figure 12. Comparison between the experimental and theoretical site-specific Al K ELNES of YAG. The dots and lines were obtained as described in the caption of figure 6.

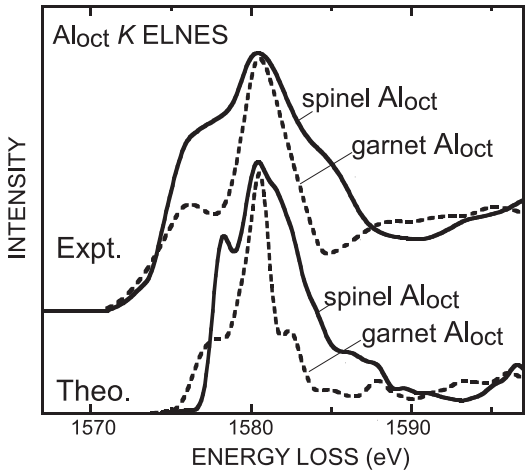

Figure 13. Comparison between experimental (upper) and theoretical (lower) Al_{oct} K ELNES profiles of $NiAl_2O_4$ and YAG.

Table 1. Atom species and coordination numbers of the first, second and third neighbor shells around the Al^*_{oct} of $NiAl_2O_4$ and YAG.

	First shell (0.19 nm)	Second shell (0.29 nm)	Third shell (0.34 nm)
$NiAl_2O_4$	O × 6	Al_{oct} × 2, Ni × 4	Al_{tet} × 6
YAG	O × 6	None	Al_{tet} × 6, Y × 6

structure containing relatively lower-energy Al_{tet} 3p states formed by significant bonding interactions among the d–p hybridized states of $\{Al_{tet}O_4\}$ units. Since the calculated 1s level of the Al_{oct} is only 0.2 eV lower than that of the Al_{tet}, the chemical shift between the different sites can be said to play a minor role.

5. Advanced applications

5.1. Comparison of site-specific Al K ELNES between spinel and garnet

$NiAl_2O_4$ has a partially inverse spinel structure where tetrahedrally and octahedrally coordinated Al atoms (Al_{tet} and Al_{oct}) are alternately arranged on the {400} planes, while a garnet structure of YAG has alternating $Al_{tet} + Al_{oct}$ and Al_{tet} planes of {400}, as shown in figure 5(b). We obtained site-specific Al K ELNES of a single-crystalline YAG grown by the Bridgeman method, in a manner similar to the case of $NiAl_2O_4$ [1]. In figure 12, the results are compared with the corresponding theoretical results. As in the case of $NiAl_2O_4$, the main peak of the Al_{oct} spectrum is at a higher energy than Al_{tet}. Thus, the discussion in the previous section is also applicable to YAG. The experimental Al_{tet} K ELNES of YAG seems in less agreement with the theoretical results, which is due to the multiple-loss effect at the relatively thicker area. We focus our discussion on the differences between the Al_{oct} K ELNES, commonly encountered in the experimental and theoretical spectra. Interestingly, YAG has a relatively sharper main peak of the octahedral spectra in both the experimental and theoretical spectra. In figure 13, we reproduce the experimental and theoretical Al_{oct} K ELNES of $NiAl_2O_4$ and YAG shown in figures 9 and 12, respectively, for a better comparison (with the energies shifted so that the main peak positions are aligned).

Because Al_{oct} has similar oxygen coordination environments in $NiAl_2O_4$ and YAG and because interactions between cationic orbitals are predominant at the high energies corresponding to the main peaks of Al_{oct} K ELNES, the width of the main peak could be ascribed to orbital interactions between the cations whose arrangements differ between these two compounds. In order to correctly identify the electronic origin of the difference in ELNES between Al with similar oxygen coordination, we will investigate theoretical electronic structures with a core-hole Al at the octahedral site (Al^*_{oct}).

Figure 14 correlates the theoretical Al_{oct} K ELNES (figures 14(a) and (d)) with the local electronic structures around Al^*_{oct}, which are represented by local densities of states (LDOS) of the near-neighbor atoms (figures 14(b) and (e)) and OPD between Al^*_{oct} 3p and the neighboring atoms (figures 14(c) and (f)). The atom species and coordination numbers of the first, second and third neighbor shells around the Al^*_{oct} of $NiAl_2O_4$ and YAG are shown in table 1, in which the shell radii are indicated.

Figures 14(b) and (e) illustrate that oxygen LDOS (first shell) is small, while cation DOSs (second and third shells) exhibit significant intensities (there are no cations in the second shell of YAG) in both structures. A comparison of the Al_{oct} K ELNES in figure 14(a) with LDOS in figure 14(b) and OPD in figure 14(c) suggests that the small shoulder around 5 eV

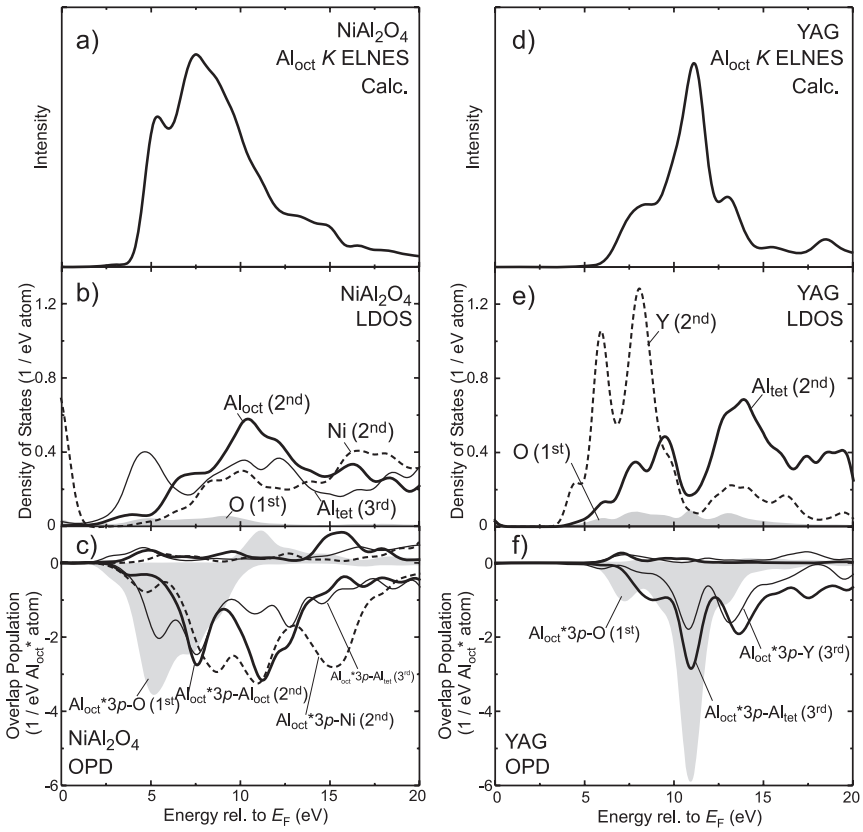

Figure 14. Theoretical analysis of Al_{oct} K ELNES of $NiAl_2O_4$ (left column) and YAG (right column) ($*$ stands for core hole): theoretical Al K ELNES (a) and (d), LDOS of neighboring atoms around Al^*_{oct} (b) and (e). Overlap population diagram (OPD) between Al^*_{oct} and its neighboring atoms (c) and (f).

in the ELNES of $NiAl_2O_4$ corresponds to the anti-bonding orbitals between Al^*_{oct} and the nearest O, and the main peak around 8 eV and the subsequent shoulders correspond to those between Al^*_{oct} and the second shell Al_{oct} and Ni. In the case of YAG, anti-bonding interactions between Al^*_{oct} and the nearest O are predominant in the main peak of the ELNES around 11 eV. The LDOSs of Al_{tet} and Y have larger intensities than that of O, though the interactions between Al^*_{oct} and the third shell cations (Al_{tet} and Y) are weaker than that between Al^*_{oct} and O, so that these interactions do not affect the ELNES that much. Therefore, the weaker interactions between the constituent cations give rise to a sharp peak in Al_{oct} K spectra of YAG.

5.2. *Ce $M_{4,5}$ ELNES of $Ce_2Zr_2O_{7.5}$*

As an application of site-specific EELS to real materials, the valence states of Ce in $Ce_2Zr_2O_{7.5}$ were studied [6]. $Ce_2Zr_2O_X$ ($X = 7$, 7.5, 8) have $2 \times 2 \times 2$ superlattices of the unit cell of a fluorite structure, in which Ce and Zr are ordered. This material is used as a catalytic promoter for reactions cleaning automotive exhaust gases. At $X < 8$, it contains oxygen vacancies (V_O) on the sublattice of anion sites coordinated by four Zr. At $X = 7$, all the sublattice sites are unoccupied. At $X = 7.5$, four V_O are ordered as shown in figure 5(c). Thus, at this composition, we have fully oxygen-occupied planes (O-filled planes) and V_O-containing planes (O-deficient planes) on alternate {200} planes. $Ce_2Zr_2O_{7.5}$ was obtained by exposing $Ce_2Zr_2O_7$ powder to air at room temperature for over 1 year [31]. The initial $Ce_2Zr_2O_7$ powder was prepared by the co-precipitation method [32]. The sample powder was dispersed on a carbon microgrid film, and observed using a 300 kV electron microscope (Hitachi H-9000NAR) equipped with a GATAN imaging filter.

Figure 15 shows the results of Ce $M_{4,5}$ spectra under (200) channeling conditions, together with those of $Ce_2Zr_2O_X$ ($X = 7$, 7.5, 8) measured in a non-channeling TEM mode. The profile of the spectrum of $Ce_2Zr_2O_{7.5}$ measured at $s_{200} > 0$ is similar to that of $Ce_2Zr_2O_7$, while that of $Ce_2Zr_2O_{7.5}$ for $s_{200} < 0$ resembles that of $Ce_2Zr_2O_8$. We repeated the measurements at the same area by changing s and confirmed that the observed changes were brought about by the diffraction condition change, rather than radiation damage such as oxygen desorption.

In the crystal structure of $Ce_2Zr_2O_{7.5}$, which has been well established by x-ray and electron diffraction measurements, Ce has only one crystallographic site in the fcc unit cell [32]. Since a negative (positive) s_{200} localizes the incident electron between the O-filled (O-deficient) plane and the Ce plane, according to the dynamical electron scattering calculations [6], the spectra under (200) plane channeling conditions reveal that a single cerium ion has a double-faced state, where two kinds of Ce states similar to those of Ce in $Ce_2Zr_2O_7$ and $Ce_2Zr_2O_8$ face in opposite directions.

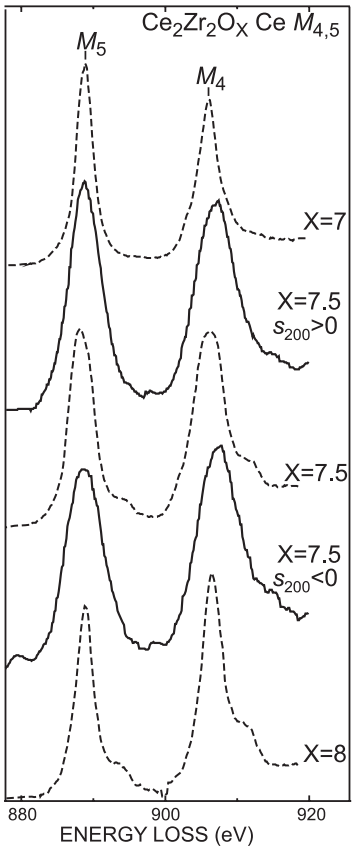

Figure 15. Ce $M_{4,5}$ of $Ce_2Zr_2O_{7.5}$ under (200) channeling conditions (solid), Ce $M_{4,5}$ of $Ce_2Zr_2O_X$, ($X = 7, 7.5, 8$) under the TEM mode (dashed).

In order to identify the cause of the marked variation in the Ce $M_{4,5}$ spectral profiles with the channeling conditions, we calculated the atomic and electronic structures of this phase by the PAW band method within the generalized gradient approximation [33] partly including a Hubbard-type orbital-dependent interaction [34, 35] for Ce 4f states (GGA + U). The theoretically optimized crystal structure coincided almost exactly with the structure obtained experimentally. This is the reason why we think the underlying theoretical electronic charge density could correctly reproduce the real electronic charge density. In the case of $Ce_2Zr_2O_{7.5}$, the huge number of configuration interactions between Ce 3d, 4f and O 2p electrons should be taken into consideration for the many-electron spectral calculation employed in the case of Mn $L_{2,3}$ spectra of Mn_3O_4 in section 3.1 because the number of electrons in the configurations must be an integer and the smallest possible cluster centering Ce cannot satisfy this condition for the composition ($Ce_2Zr_2\underline{O_{7.5}}$). We just calculated the electron charge distribution by the PAW method within the GGA + U framework. The effective U was set to 2.5 eV, which was reported to provide reasonable agreement with the experimental formation energies of Ce_2O_3 and CeO_2 [36]. Moreover, for the $Ce_2Zr_2O_7$ reduced phase, our calculated energy gap between the occupied Ce 4f state and the bottom of the conduction bands is 0.6 eV, which seems in agreement with the experimental activation energy (∼0.5 eV) of the electric conduction [37].

Figure 16 shows the local electronic and atomic structures around Ce. As depicted in figure 16(b), Ce is located on the threefold symmetry axis in the cubic system, coordinated by four kinds of oxygen atoms at different crystallographic sites (O_{1-4}). Among the oxygen atoms, O_4 is the nearest neighbor to V_O and significantly displaced toward V_O from the symmetric tetrahedral coordination position. We evaluated the effective ionic charges by Bader's method [38]. They were −0.4, −1.2, −1.2 and −2.0 for O_1 to O_4, indicating a strongly anisotropic charge distribution along the threefold axis. In figure 16, these ions were colored darker in the order of decreasing effective charge. The significantly displaced oxygen atoms, O_4, were most ionic, as if restoring the original Madelung potential of the fluorite structure.

Because of the anisotropy in the electron charge and atomic positions, the local structure around Ce looks very different on either side separated by a plane perpendicular to the threefold axis (shown as a gray plane in figure 16(b)). The one side, containing O_3 and O_2, has relatively short Ce–O distances and the Ce 4f charge in figure 16(a) is rather delocalized between O_2 and Ce. On the other side, the Ce 4f charge is rather localized at Ce. If the real Ce 4f electron is as delocalized as the calculation suggests, the charge density of the band calculation is likely compatible with the double-faced state deduced from the experimental Ce $M_{4,5}$ spectral profiles.

For a further discussion on the relationship between the Ce 4f charge distribution and the spectral profile, let us examine the fine structures of Ce $M_{4,5}$. The TEM-mode spectra of $Ce_2Zr_2O_8$ and $Ce_2Zr_2O_{7.5}$ exhibit small shoulders approximately 5 eV above the M_4 and M_5 main peaks. In the spectra obtained under channeling conditions, although a lower-energy resolution smears out the fine structures, the spectrum at $s_{200} < 0$ does exhibit more distinct shoulder structures than that at $s_{200} > 0$. Kotani *et al* interpreted the fine structures of Ce $M_{4,5}$ x-ray absorption spectra (XAS) of CeO_2 and CeF_3 using the Anderson impurity model [39]. This model also explained Ce 4f to 3d resonant x-ray fluorescence spectra [40]. According to the model, the shoulder structures that appeared in Ce $M_{4,5}$ XAS of CeO_2 are due to the mixed valence state of Ce: the ground state $|\mathbf{g}\rangle$ is a mixed valence state consisting of a Ce 4f electron and an O 2p valence hole, $|\mathbf{g}\rangle = a|f^0\rangle + b|f^1\underline{v}\rangle$. Similarly, the final states of Ce $M_{4,5}$ XAS are given by $c|\underline{d}f^1\rangle + d|\underline{d}f^2\underline{v}\rangle$ and $d'|\underline{d}f^1\rangle - c'|\underline{d}f^2\underline{v}\rangle$ for the main peak and shoulder, respectively. Thus, the shoulder structures of CeO_2 are derived from the strong covalency hybridization between Ce 4f and O 2p states. By contrast, the spectral profile of CeF_3 simply reflects the trivalent state of Ce, $|\mathbf{g}\rangle = |f^1\rangle$ and $|\mathbf{f}\rangle = |\underline{d}f^2\rangle$. The more detailed structures in the spectra of CeO_2 and CeF_3 are well reproduced by the multiplets of the final state configuration. Since the spectral profiles of $Ce_2Zr_2O_8$ and $Ce_2Zr_2O_7$ are very similar to those of CeO_2 and CeF_3, respectively, we can deduce the novel valence state of Ce in $Ce_2Zr_2O_{7.5}$, in which Ce 4f and O 2p are strongly hybridized and form a '*mixed valence state*' on the O-rich side and the Ce 4f electron is localized and forms a '*trivalent state*' on the O-deficient side. The Ce 4f charge density of the DFT-based calculation in figure 16(a) can be interpreted as the spatially smoothed charge density of this valence state.

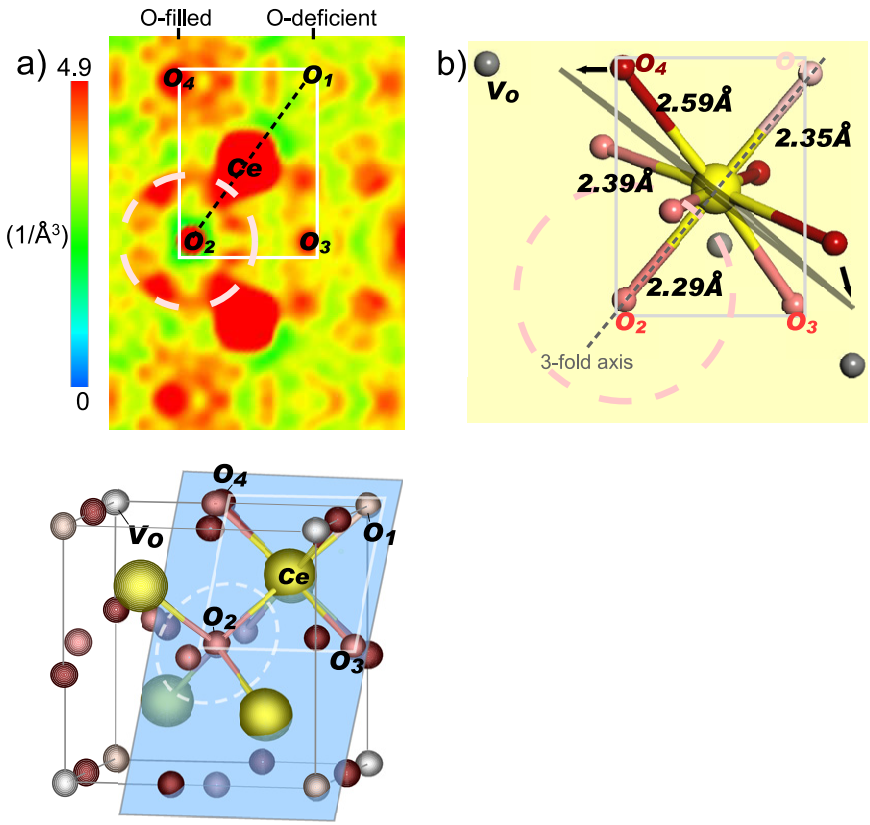

Figure 16. (a) GGA + U charge density of Ce 4f states ((a) upper) on the plane shown in (a) lower. The lower part shows an octant of the unit cell of $Ce_2Zr_2O_{7.5}$. (b) Local atomic arrangement around Ce. The rectangle and circle shown in (a) are indicated again.

6. Summary and concluding remarks

In the present paper, we give an overview of the historical background, the present status of the sophisticated combination of TEM-EELS and first-principles electronic calculations for site-selective electronic states in crystalline materials, exploiting electron channeling phenomena, and advanced application examples investigated recently by the present authors' group. The main results can be summarized as follows.

(1) The site-selective ELNES measurements first applied to spinel structures, in which the two anion sites differently coordinated by oxygen (tetrahedral (T-site) and octahedral sites (O-site)) are aligned on alternating {400} planes. The experimental ELNES of the fine structure varied consistent with the weighted sum of the theoretical spectra of the T- and O-sites, the two components predominating alternately as the sign of the excitation error near the {400} Bragg condition is changed. These findings showed that the combination of site-specific ELNES measurements and reliable first-principles calculations will be useful to determine the charge ordering in the transition metal materials.

(2) Data processing techniques effective for the site-selective ELNES are introduced: multivariate curve resolution (MCR) applied to the systematic ELNES data measured with the excitation errors systematically varied, which successfully restored the pure spectral components and their relative compositions from the data set. In addition, the signal restoration method based on the Pixon algorithm removed the statistical noise from the site-specific experimental spectra with low SNR, which enabled us to better compare the experimental fine structures with theoretical ones. Site-selective ELNES measurements were fulfilled in the true sense of the word, with the aid of state-of-the-art data processing.

(3) The above-mentioned method we developed has opened up the possibility of discussing spatially localized electronic structures: the main peak positions in the Al_{oct} and Al_{tet} K ELNES of $NiAl_2O_4$ inverse spinel were interpreted in terms of the conduction-band structures.

(4) Site-specific Al K spectra of a garnet structure and $NiAl_2O_4$ spinel were discussed, in which the local coordinations farther than the first nearest neighbors are different from each other: the position and shape of the main peak of Al_{oct} ELNES were compared between the two structures; the difference was found to be ascribable to the local atomic arrangement around Al_{oct}.

(5) $Ce_2Zr_2O_{7.5}$, used as a catalytic promoter, was analyzed by site-specific EELS. The Ce $M_{4,5}$ profiles changed significantly depending on whether the incident electron propagated along the oxygen-deficient plane or along the oxygen-rich plane. The first-principles DFT + U calculation indicated strongly anisotropic charge distribution along the threefold axis in the cubic system.

The site-specific ELNES revealed a novel valence state of Ce in $Ce_2Zr_2O_{7.5}$, in which Ce 4f and O 2p are strongly hybridized and form a '*mixed valence state*' on the O-rich side and the Ce 4f electron is localized and forms a '*trivalent state*' on the O-deficient side.

Finally, we would like to make several remarks on further improvements to the method. One of the technical shortcomings of this method is the low S/N due to the off-axis geometrical configuration of measurements. Prolonged measurements would improve S/N considerably if the inevitable energy drift due to instrumental instabilities during measurement is corrected for. We have recently developed a program script working on DigitalMicrograph™ that corrects the energy drift online [41]. This will improve the data quality of our future experiments.

Another goal is to open up the possibility for quantitative measurements, such as occupancy determination of cations with different valencies. To achieve this, the theoretical formulation given in section 2 must be extended to the more general many-beam case, and automated EELS measurements in which the beam incident angle is digitally controlled are necessary to apply the MCR technique effectively.

Further applications are planned to extend site-specific electronic structure analysis to various kinds of materials, such as layered solid solution thin films and spinel ferrite materials, both of which exhibit interesting electronic and magnetic properties and high-pressure crystalline phases that *are* formed on the same element with different coordination.

The present authors are developing a new wavelength-dispersive x-ray (WDX) spectrometer for TEM to perform soft-x-ray emission spectroscopy (SXES) [42]. This WDX-SXES system covers 150–2500 eV of x-ray emission energy with an energy resolution comparable to that of TEM-EELS. We have started SXES experiments under channeling conditions to obtain site-selective PDOS of occupied states, which will play a very important and complementary role when combined with channeling TEM-EELS.

Acknowledgments

The present work was partly supported by a Grant-in-Aid for Scientific Research of MEXT, Japan (Kibankenkyu A: 17206063 and Priority Area (No 474) 'Atomic scale modification'), JSPS (Wakate B: 16760531 and 18760493) and the DAIKO Foundation. The authors thank Professor W Y Ching of the University of Missouri—Kansas City for allowing us to use the OLCAO code.

References

[1] Yamamoto Y, Tatsumi K and Muto S 2007 *Mater. Trans.* **48** 2590
[2] Tatsumi K, Muto S, Yamamoto Y, Ikeno H, Yoshioka S and Tanaka I 2006 *Ultramicroscopy* **106** 1019
[3] Taftø J and Krivaneck O L 1982 *Phys. Rev. Lett.* **48** 560
[4] Leifer K and Buffat P A 1997 *Inst. Phys. Ser.* **157** 381
[5] Self P G and Buseck P R 1983 *Phil. Mag.* A **48** L21
[6] Arai S, Muto S, Sasaki T, Tatsumi K, Ukyo Y, Kuroda K and Saka H 2005 *Solid State Commun.* **135** 664
[7] Gloter A, Douiri A, Tence M and Colliex C 2003 *Ultramicroscopy* **96** 385
[8] Kimoto K, Ishizuka K, Mizoguchi T, Tanaka I and Matsui Y 2003 *J. Electron Microsc.* **52** 299
[9] Kuzuo R and Tanaka M 1993 *J. Electron Microsc.* **42** 240
[10] Tanaka I, Mizoguchi T and Yamamoto T 2005 *J. Am. Ceram. Soc.* **88** 2013
[11] Schattschneider P 1986 *Fundamentals of Inelastic Electron Scattering* (New York: Springer)
[12] Kohl H and Rose H 1985 *Adv. Electron. Electron Phys.* **65** 173
[13] Schattschneider P, Nelhiebel M, Schenner M, Grogger W and Hofer F 1996 *J. Microsc.* **183** 18
[14] Schattschneider P, Jouffrey B and Nelhiebel M 1996 *Phys. Rev.* B **54** 3861
[15] Hirsch P, Howie A, Nicholson R, Pashley D W and Whelan M J 1977 *Electron Microscopy of Thin Crystals* (Malabar, FL: Krieger) chapter 8
[16] Boucher B, Buhl R and Perrin M 1971 *J. Phys. Chem. Solids* **32** 2429
[17] Jensen G and Nielsen O 1974 *J. Phys. C: Solid State Phys.* **7** 409
[18] Ogasawara K, Iwata T, Koyama Y, Ishii T, Tanaka I and Adachi H 2001 *Phys. Rev.* B **64** 115413
[19] Ikeno H and Tanaka I 2008 *Phys. Rev.* B **77** 075127
[20] Williams D B and Carter C B 1996 *Transamission Electron Microscopy II* (New York: Springer) p 223
[21] Roelofsen J N, Peterson R C and Raudsepp M 1992 *Am. Mineral.* **77** 522
[22] Ching W Y 1990 *J. Am. Ceram. Soc.* **73** 3135
[23] Mo S D and Ching W Y 2000 *Phys. Rev.* B **62** 7901
[24] Mizoguchi T, Tatsumi K and Tanaka I 2006 *Ultramicroscopy* **106** 970
[25] Kresse G and Joubert D 1999 *Phys. Rev.* B **59** 1758
[26] Kresse G and Furthmüller J 1996 *Phys. Rev.* B **54** 11169
[27] Tauler R and Kowalski B 1993 *Anal. Chem.* **65** 2040
[28] Wang J H, Hopke P K, Hancewicz T M and Zhang S L 2003 *Anal. Chim. Acta* **476** 93
[29] Muto S, Puetter R C and Tatsumi K 2006 *J. Electron Microsc.* **55** 215
[30] Muto S, Tatsumi K, Puetter R C, Yoshida T, Yamamoto Y and Sasano Y 2006 *J. Electron Microsc.* **55** 225
[31] Sasaki T, Ukyo Y, Suda A, Sugiura M, Kuroda K, Arai S and Saka H 2003 *J. Ceram. Soc. Japan* **111** 382
[32] Sasaki T, Ukyo Y, Kuroda K, Arai S, Muto S and Saka H 2004 *J. Ceram. Soc. Japan* **112** 440
[33] Perdew J P, Burke K and Ernzerhof M 1996 *Phys. Rev. Lett.* **77** 3865
[34] Anisimov V I, Solovyev I V, Korotin M A, Czyzyk M T and Sawatzky G A 1993 *Phys. Rev.* B **48** 16929
[35] Dudarev S L, Botton G A, Savrasov S Y, Humphreys C J and Sutton A P 1998 *Phys. Rev.* B **57** 1505
[36] Loschen C, Carrasco J, Neyman K M and Illas F 2007 *Phys. Rev.* B **75** 035115
[37] Baidya T, Hegde M S and Gopalakrishnan J 2007 *J. Phys. Chem.* B **111** 5149
[38] Bader R F W 1990 *Atoms in Molecules—a Quantum Theory* (New York: Oxford University Press)
[39] Ogasawara H, Kotani A, Okada K and Thole B T 1991 *Phys. Rev.* B **43** 854
[40] Butorin S M, Mancini D C, Guo J-H, Wassdahl N, Nordgren J, Nakazawa M, Tanaka S, Uozumi T, Kotani A, Ma Y, Myano K E, Karlin B A and Shuh D K 1996 *Phys. Rev. Lett.* **77** 574
[41] Sasano Y and Muto S 2009 *J. Electron Microsc.* **57** 149
[42] Muto S, Tatsumi K and Takahashi H 2008 *Proc. 14th European Microscopy Congress (Aachen, Sept. 2008)* pp 575–6